Journal of Micromechanics and Microengineering

PAPER

Performance enhance of CMOS-MEMS thermoelectric infrared sensor by using sensing material and structure design

IOP Publishing Journal of Micromechanics and Microengineering
J. Micromech. Microeng. **29** (2019) 025007 (15pp) https://doi.org/10.1088/1361-6439/aaf7dd

Performance enhance of CMOS-MEMS thermoelectric infrared sensor by using sensing material and structure design

Ting-Wei Shen[1], Kai-Chieh Chang[3], Chih-Ming Sun[4] and Weileun Fang[1,2]

[1] Institute of NanoEngineering and MicroSystems, National Tsing Hua University, Hsinchu, Taiwan
[2] Power Mechanical Engineering, National Tsing Hua University, Hsinchu, Taiwan
[3] Asia Pacific Microsystems, Inc., Hsinchu Science Park, Hsinchu, Taiwan
[4] PixArt Imaging Inc., Hsinchu Science Park, Hsinchu, Taiwan

E-mail: fang@pme.nthu.edu.tw

Received 21 September 2018, revised 30 November 2018
Accepted for publication 11 December 2018
Published 3 January 2019

Abstract

This study presents the micro thermoelectric infrared (IR) sensor consisting of the heat transduction absorber and the serpentine structure with embedded thermocouple using the TSMC 0.18 μm 1P6M standard CMOS process and the in-house post-CMOS MEMS process. The proposed IR absorber design has an umbrella-like structure with a post anchor to the serpentine suspension with embedded thermocouple. Compared to the reference design (IR sensor consisted of only the serpentine structure with embedded thermocouple), a better heat-flow path is achieved and the temperature difference between the hot and cold junctions is increased. Moreover, the umbrella-like structure has higher IR absorption area compared with the serpentine structure. In addition, the Seebeck coefficients of poly-Si films with and without silicide are respectively characterized. The poly-Si with no silicide has a much higher Seebeck coefficient (56-fold), and is employed in this study as the thermocouple material. Experiment results indicate the detectivity of proposed design is 2–2.6 fold higher than that of the reference one at 200 mTorr. Experiment also show that the responsivity enhancement of proposed design is further increased as the sensor size is reduced in area.

Keywords: CMOS-MEMS, thermoelectric, Seebeck effect, thermopile, infrared sensor

(Some figures may appear in colour only in the online journal)

1. Introduction

The infrared (IR) sensors have been extensively applied to military and consumer electronics including night vision device, thermal imager, non-contact temperature measurement tool, human behavior detection system, etc. The sensing approaches of IR sensors generally can be categorized as photon detection and thermal detection (uncooled IR sensor). Despite of the advantages of high resolution, signal-to-noise performance, and fast response time, the photon detector needs to equip with a bulky and expensive cooling system. The uncooled IR detectors absorb the incoming IR radiation to change the material temperature, and further cause the change of various temperature-dependent properties to generate the electrical output [1–3]. Thus, the thermal detection IR sensor could operate at room temperature, and hence the cooling system is not required and the size and cost can be reduced [4]. In this regard, the thermal IR sensors are appropriate for various applications such as the consumer electronics, the IoT (internet of things), and the Industry 4.0 [5].

There are three major sensing mechanisms for the thermal IR detectors including, the pyroelectric, thermal-resistant, and thermoelectric effects [2]. To leverage available foundry processes for device implementation, the thermoelectric type IR sensor is investigated in this study. The sensing mechanism of thermoelectric IR sensors is based on the Seebeck effect, which can generate the voltage output by the temperature difference of thermoelectric material [6–8]. As compared with bolometer and pyroelectric sensor, the thermoelectric one has advantages of low power consumption and no flicker noise [9,

10]. However, the thermoelectric IR sensor has various design concerns such as the relatively low responsivity, and the challenge to reduce device footprint [4]. The thermal couple is designed to increase the temperature different between hot and cold junctions to further improve the performance of thermoelectric IR sensors [11]. Meanwhile, the device footprint is also increased for this design. The structure and thermocouple design in [12, 13] could increase the responsivity of sensor without changing the footprint of device. It is also possible to employ the sensing material (such as doped Si or poly-Si) with higher figure of merit to improve the performance of IR sensor [14].

The standard CMOS (complementary metal-oxide semiconductor) processes are mature fabrication technologies available in many foundries. The CMOS processes could offer the stacking of many thin films for the design of MEMS structures and electrical routings. By adding additional processes (post-CMOS processes) on the CMOS chip from foundry, the monolithic integration of the integrated circuit (IC) and MEMS structures is achieved [15–17]. The CMOS-MEMS processes have been employed to implement inertial sensors [18], microphones [19], pressure sensors [20], and tactile sensors [21], etc. Moreover, various CMOS-MEMS thermoelectric IR sensors have also been demonstrated [22–27]. By using the available CMOS thin film materials and layers stacking, the performance of thermoelectric IR sensor has been improved through the designs of thermocouple [22, 23] and structures [7, 12, 13, 27, 28]. To enhance the performance of the CMOS-MEMS thermoelectric IR sensor, this study proposed the design of an umbrella-like structure as an IR absorber. Moreover, the Seebeck coefficient of available CMOS thin films (the poly-Si (N^+/P^+) films with and without silicide) are evaluated and then selected as sensing materials for thermocouple. Based on the TSMC (Taiwan Semiconductor Manufacturing Corp.) 0.18 μm 1P6M (one poly-Si layer and six metal layers) standard CMOS processes, the proposed IR sensor is designed and implemented.

2. Concept and design

This study exploits the TSMC 0.18 μm 1P6M standard CMOS process to fabricate the thermoelectric IR sensor. Thus, the proposed sensor needs to follow the design rules provided by the CMOS foundry, and the device design is limited by the available thin film materials. In this study, the poly-Si layer doped with N^+/P^+ is used as the sensing material, and the six metal/dielectric layers is employed to construct suspended mechanical structures and the electrical routings. Moreover, various important parameters for thermoelectric IR sensor such as the responsivity (R_s), the noise equivalent power (NEP), and the specific detectivity (D^*) are considered in the proposed design for performance enhancement.

2.1. Design considerations

The thermal type IR sensor absorbs the incoming IR radiation to change the temperature of sensing materials for thermocouple, as shown in figure 1(a). The power (P_{net}) received by sensor through the IR radiation can be determined as,

$$P_{net} = \epsilon\sigma A\left(T_1^4 - T_0^4\right) \tag{1}$$

where ε is the emissivity, σ is the Stefan–Boltzmann constant (5.6697×10^{-8} W m^{-2} K^{-4}), A is the area of absorber, T_1 is the temperature of emitter (object), and T_0 is the temperature of absorber (sensor) [29]. As indicated in figure 1(a), according to the Seebeck effect [28], the output voltage ΔV yielded from thermopile can be expressed as [23],

$$\Delta V = N\left(\alpha_1 - \alpha_2\right)\Delta T \tag{2}$$

where α_1 and α_2 are the Seebeck coefficients of two sensing materials for thermocouple, Δe is the temperature difference between hot and cold junctions, and N is the number of thermocouples in series connection. From equations (1) and (2), the responsivity (R_s), which is the criterion for transferring IR radiation energy to electric signal of thermoelectric IR sensor, can be expressed as [3],

$$R_s = \frac{V_{out}}{P_{net}\sin^2\theta} = \frac{N\left(\alpha_1 - \alpha_2\right)\Delta T}{\epsilon\sigma A\left(T_1^4 - T_0^4\right)\sin^2\theta} \tag{3}$$

where the θ is 1/2 field view of sensor. In this study, the proposed design will enhance the responsivity by increasing the temperature difference ΔT and also by varying the Seebeck coefficients α.

Moreover, the Johnson noise V_n, which is the major noise source of thermoelectric IR sensor, can be determined from [30],

$$V_n = \sqrt{4kTR\Delta f} \tag{4}$$

where k is the Boltzmann constant (1.38×10^{-23} J K^{-1}), T is the absolute ambient temperature, R is the electric resistance of sensor, and Δf is the frequency bandwidth for measurement. According to equations (3) and (4), the NEP of sensor can be expressed as [3],

$$\mathrm{NEP} = \frac{V_n}{R_s}. \tag{5}$$

Finally, this study also employed the parameter of specific detectivity (D^*) [3],

$$D^* = \frac{\sqrt{A\Delta f}}{\mathrm{NEP}} \tag{6}$$

to make fair comparisons between sensors of different sensing mechanism and size.

2.2. Device design and analysis

The structure design of the proposed IR sensor will follow the design rule of TSMC 0.18 μm 1P6M standard CMOS process. By using the mature standard CMOS process, the variation of material properties (Seebeck coefficient, emissivity, electric resistance, thermal resistance) between sensors can be reduced. This study employs the available metal, dielectric, tungsten, and poly-Si thin films to design and implement the proposed

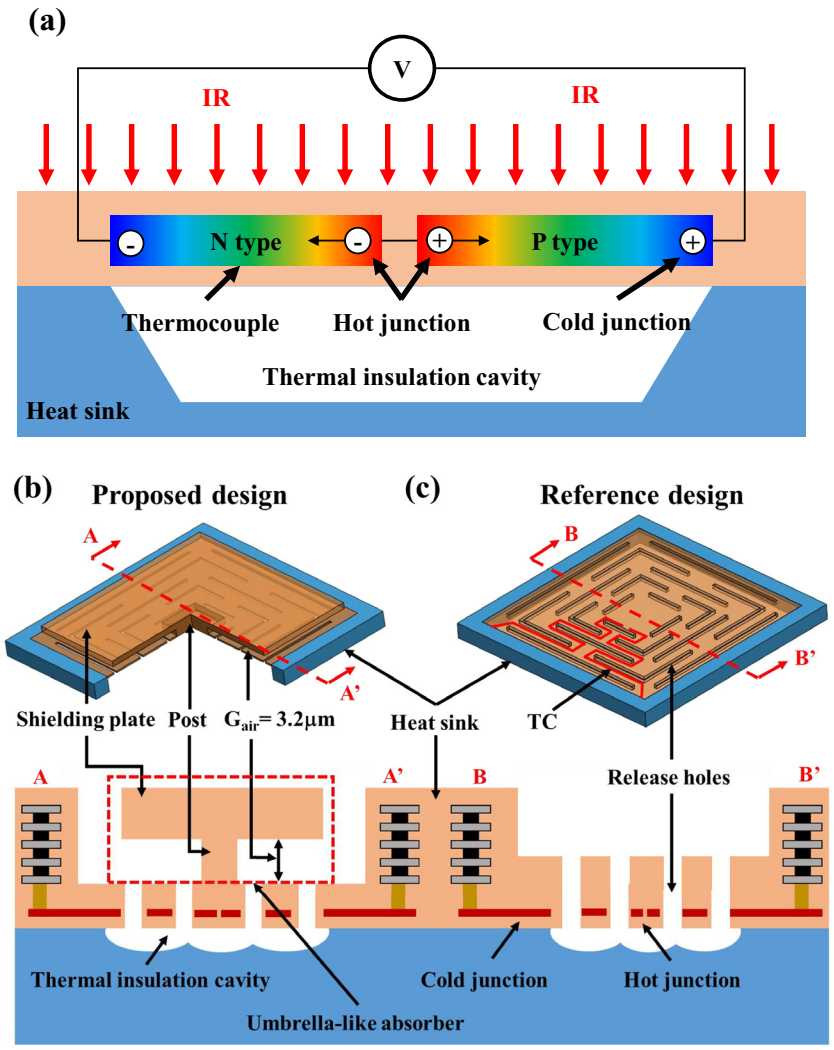

Figure 1. (a) The design concept of a thermoelectric IR sensor, (b) the schematic illustration of proposed IR sensor consisting of an umbrella-like absorber on top of the serpentine structure with embedded thermocouples, and (c) the existing design with only the serpentine structure with embedded thermocouples.

sensor. As shown in figure 1(b), the proposed thermoelectric IR sensor exploits the umbrella-like absorber (marked with dashed line in figure 1(b)) to shield the serpentine thermopile (serpentine structure with embedded thermocouples) shown in figure 1(c) [13]. The umbrella-like absorber is consisted of a shielding plate and a post, and the shielding plate is connected to the serpentine structure by using the post. In this design, the incoming photons will only incident and generate heat on the shielding plate of the absorber. Thus, the heat generated on shielding plate could only transfer to the hot junction of thermocouple underneath via the post, and the temperature of hot junction is increased. Moreover, the temperature difference (ΔT) between hot and cold junctions is also increased. Due to the consideration of thermal isolation, striped etching release holes are required for the serpentine structure in figure 1(c) [13]. In comparison, striped thermal isolation holes are not required for the shielding plate, and thus the photon absorbing area is increased for near 12% to further increase the ΔT. The finite element method (FEM) simulation (by using the commercial software, ANSYS) has been employed to confirm the design concept. The FEM model is shown in figure 2(a). To compare the temperature difference ΔT of the proposed and reference designs, the same incident heat flux and boundary condition on devices are established in the simulation models. Moreover, the heat conduction through the air is ignored (i.e. in vacuum condition). The simulation results in figure 2(b) respectively show the temperature distribution on the shielding plate of absorber (for the proposed design only) and the serpentine structure (for both proposed and reference designs). The serpentine structure for both designs are identical with the foot print of 204 × 204 μm^2. According to the simulations, the maximum temperature difference ΔT of the proposed design (0.629 K) is 2.6 times larger than that of the reference design (0.238 K). It shows the proposed design could offer the advantage of increasing the temperature difference ΔT, so as to further improve the responsivity. To further investigate the effect of device dimensions, simulation results of sensors with foot print of 120 × 120 μm^2 are shown in figure 2(c). The width and space of the serpentine structures with different footprint are the same. Since the dimensions of umbrella-like structure is reduced from 204 × 204 μm^2 to 120 × 120 μm^2, the post to support the structure is reduced

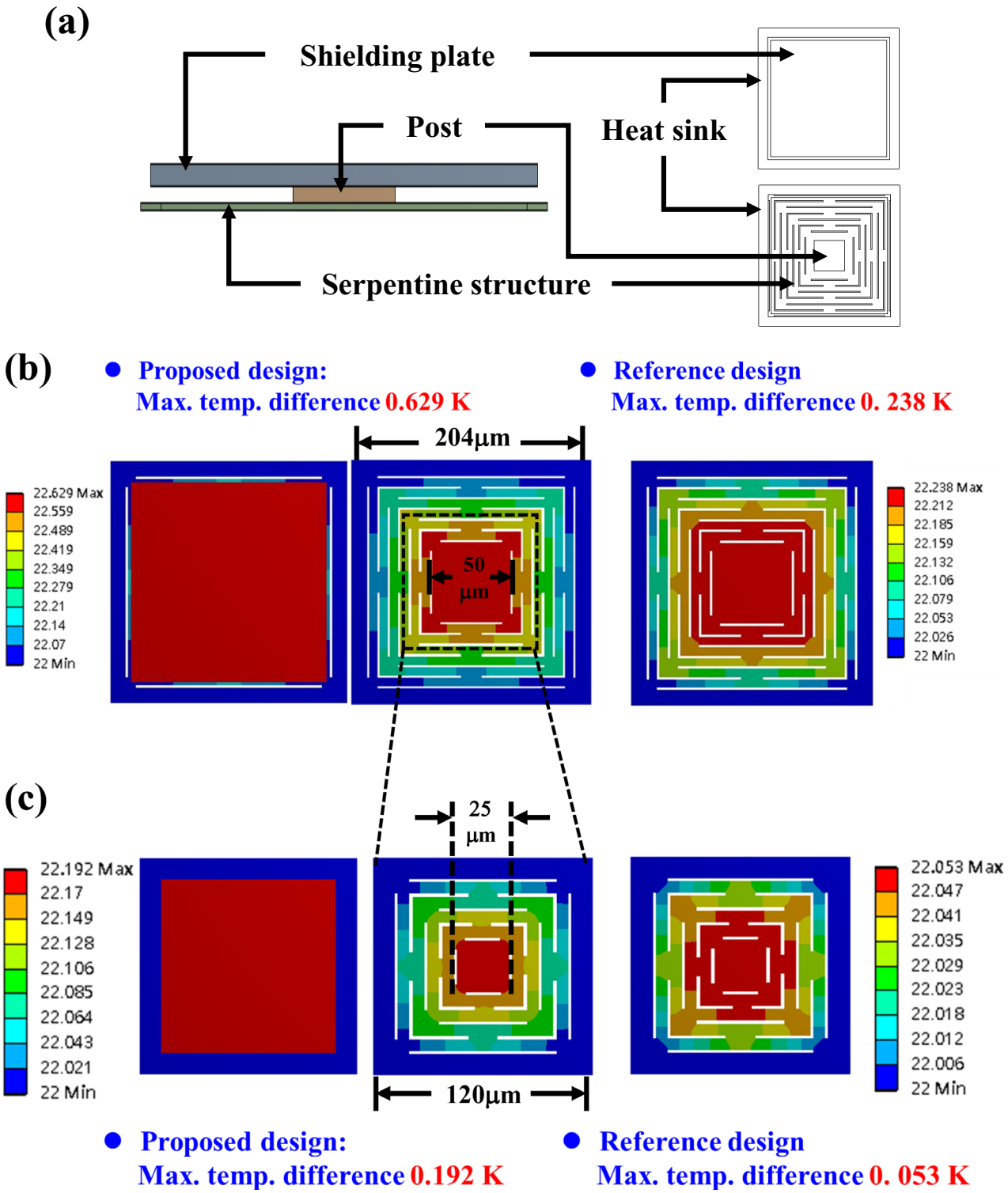

Figure 2. (a) The model for FEM simulation; and the predicted temperature distribution by FEM simulation for the proposed sensor designs with (b) 204 × 204 μm^2 footprint, (c) 120 × 120 μm^2 footprint.

from 50 × 50 μm^2 to 25 × 25 μm^2. Thus, the thermal resistant of post is increased. Simulation results show that, for sensors with 120 × 120 μm^2 footprint, the maximum temperature difference ΔT of proposed design (0.192 K) becomes 3.6 times higher than that of the reference design (0.053 K). In other words, as compare with the reference design, the advantage of proposed design is further enhanced when the sensor size is reduced in area.

Note that the suspended serpentine thermopile consisted of the CMOS layers has an initial bending due to the thin film residual stresses [31]. As the bending deformation of suspended serpentine structure exceeds the gap G_{air} shown in figure 1(b), the thermopile will contact the shielding plate of absorber and cause the change of heat-flow path and temperature difference ΔT of the sensor. As predicted by the FEM simulation, the maximum initial bending deformation of the

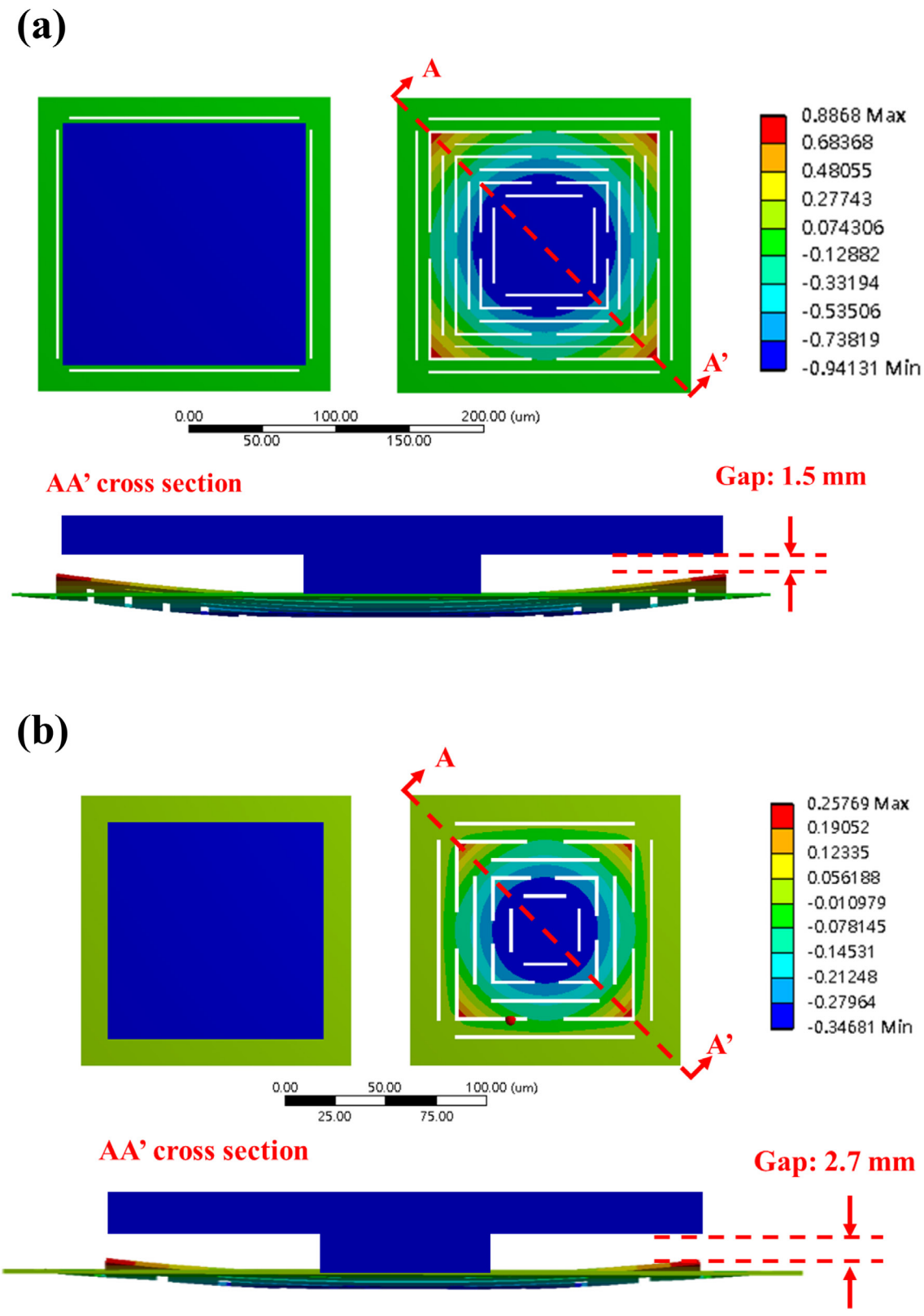

Figure 3. Simulation results of the out-of-plane deformation of the suspended serpentine structure caused by the thin film residual stresses. The cross section view also depicts the variation of the thermal isolation gap due to the bending of suspended structure. (a) The result for 204×204 μm^2 sensor, and (b) the result for 120×120 μm^2 sensor.

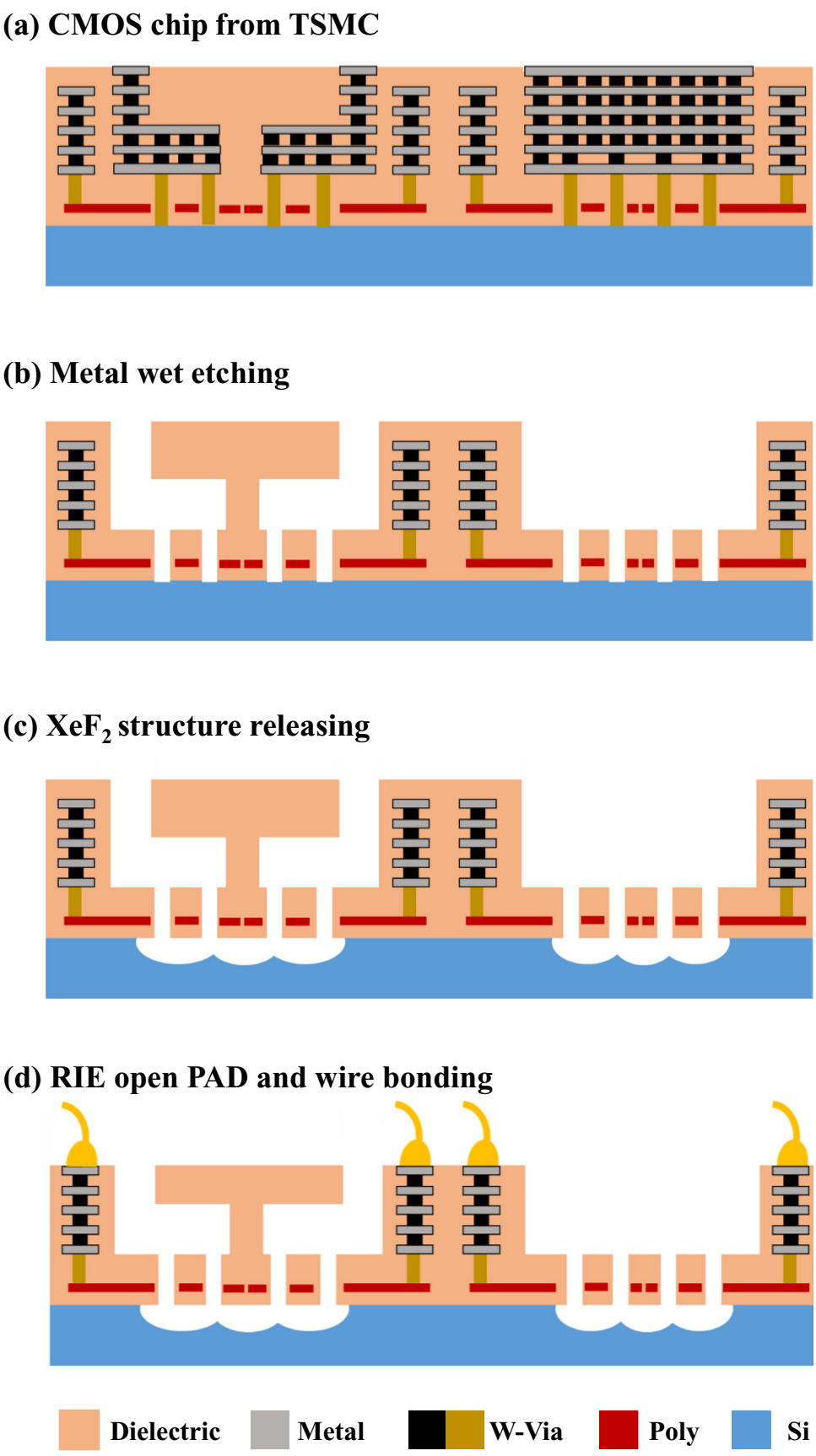

Figure 4. Fabrication process steps, (a) the CMOS chip fabricated by TSMC, (b) the metal wet etching to define the structure of sensors, (c) the XeF_2 isotropic Si etching to suspend the structure for thermal isolation, and (d) the RIE etching to remove the dielectric layer to open the bonding pad for wire-bonding.

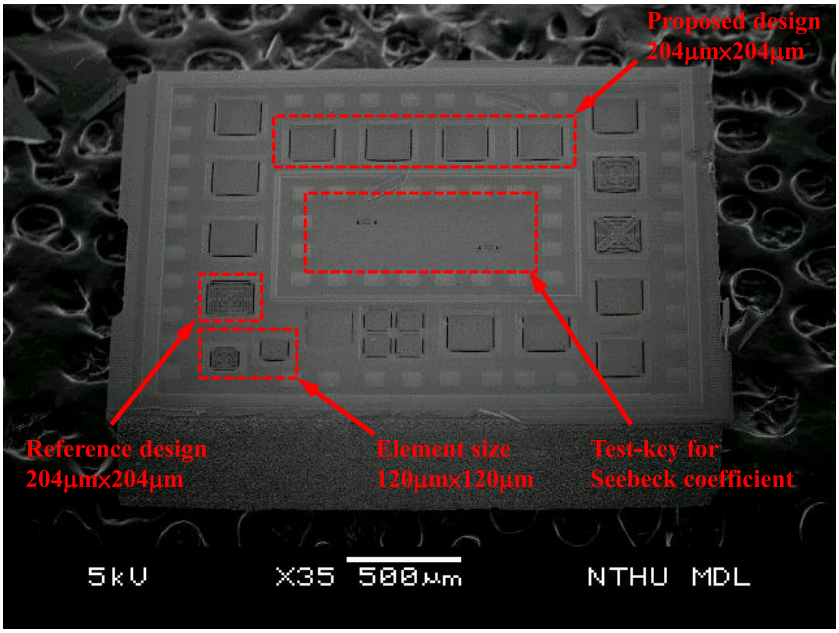

Figure 5. The SEM micrograph to display the over view of a typical fabricated chip. The chip contains the presented sensors including the proposed and reference designs with different footprints, and test-keys to characterize the Seebeck coefficient of poly-Si.

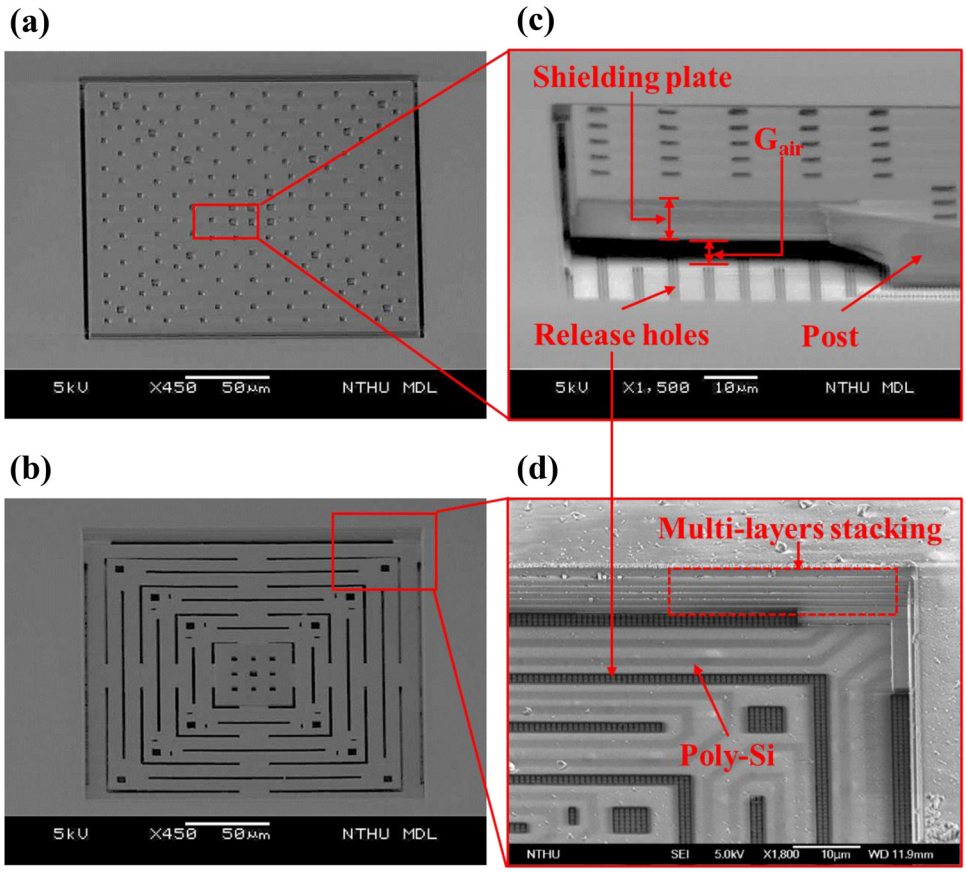

Figure 6. SEM micrographs to show more detail of fabricated IR sensors, (a) proposed design with umbrella-like absorber, (b) reference design with serpentine structure and thermocouples, (c) zoom-in cross section view of the proposed design to show the shielding plate, post, air gap, and the serpentine thermopile underneath, and (d) zoom-in micrograph to show the serpentine structure with poly-Si thermocouples.

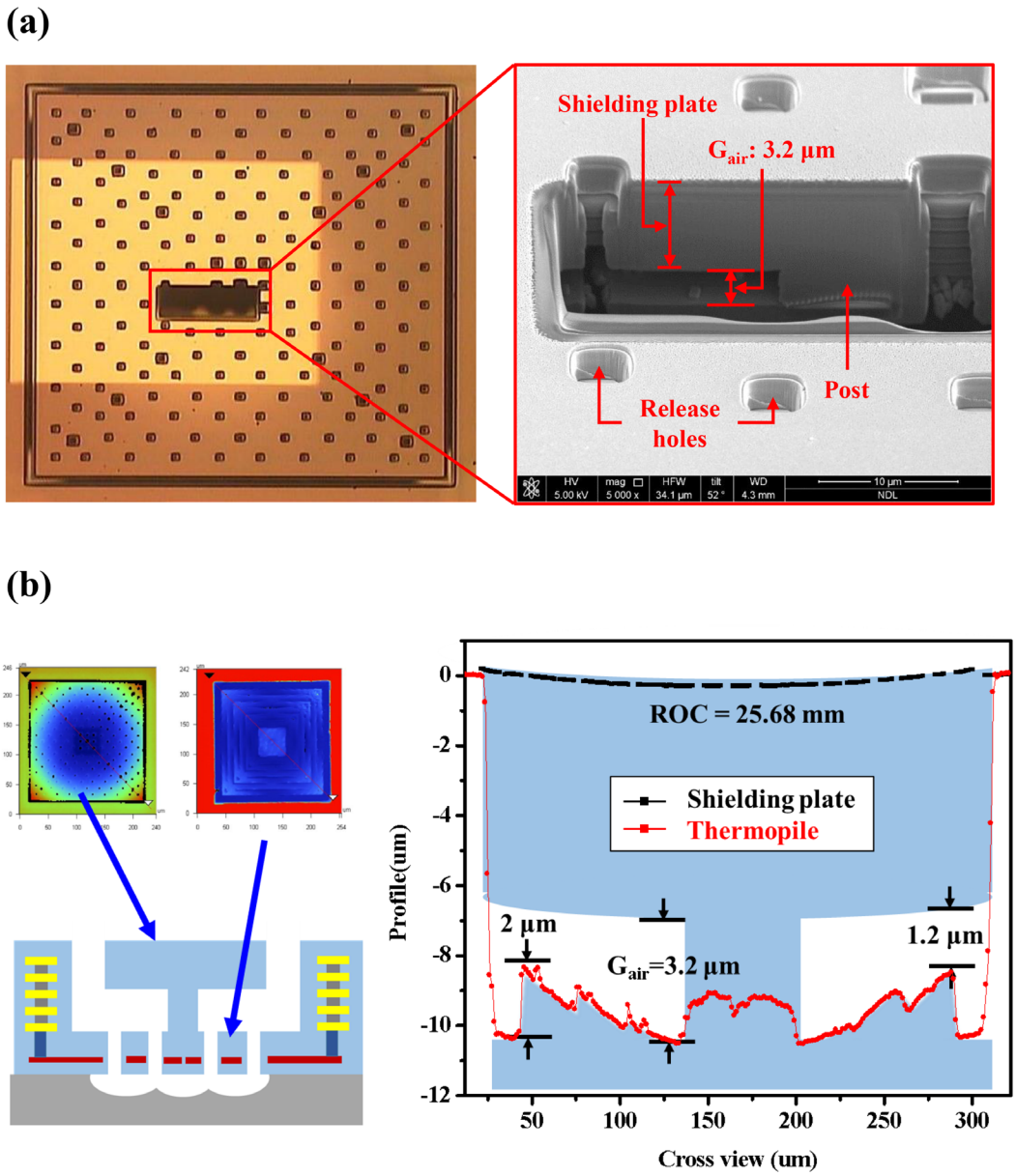

Figure 7. (a) Micrographs further show the cross section (by focused ion beam) of umbrella-like absorber, and (b) the surface profiles measured by the non-contact optical interferometer to display the initial deformation of shielding plate and serpentine structure caused by the thin film residual stresses. The result indicates that no contact between the two structures to ensure the thermal isolation by air gap.

serpentine structures with 204 × 204 μm^2 and 120 × 120 μm^2 foot prints are respectively 1.7 μm and 0.5 μm. Thus, to ensure the thermal isolation by air gap, an initial gap $G_{air} = 3.2$ μm has been designed in this study based on the available thin films in the standard CMOS process. The simulation results in figure 3 indicate the required final air gaps after processes.

3. Fabrication and results

Figure 4 displays the process steps to fabricate the proposed CMOS-MEMS thermoelectric IR sensor. Figure 4(a) shows the layers stacking and patterning of the presented device after fabricated by TSMC using the standard 0.18 μm 1P6M CMOS process. After that, the chip was fabricated using the in-house post-CMOS processes to form the MEMS structure. As shown in figure 4(b), the metal and tungsten via layers were removed by the H_2SO_4 and H_2O_2 etching solution to define the umbrella-like absorber and the underneath serpentine structures. As illustrated in figure 4(c), the serpentine thermopiles were suspended for thermal isolation after the dry bulk Si etching by XeF_2. Finally, the reactive ion etching (RIE) was employed to open the bonding pads for the following wire bonding, as shown in figure 4(d). Moreover, the presented processes also consider the figure of merit (Z) of the sensing material for the thermoelectric IR sensor [25],

$$Z = \frac{\alpha^2}{\rho\kappa}T \tag{8}$$

where ρ is electrical resistivity, κ is thermal conductivity. Thus, the sensor performance can be further improved by selecting the sensing material with a higher figure of merit from the available CMOS films. For example, the Seebeck coefficient

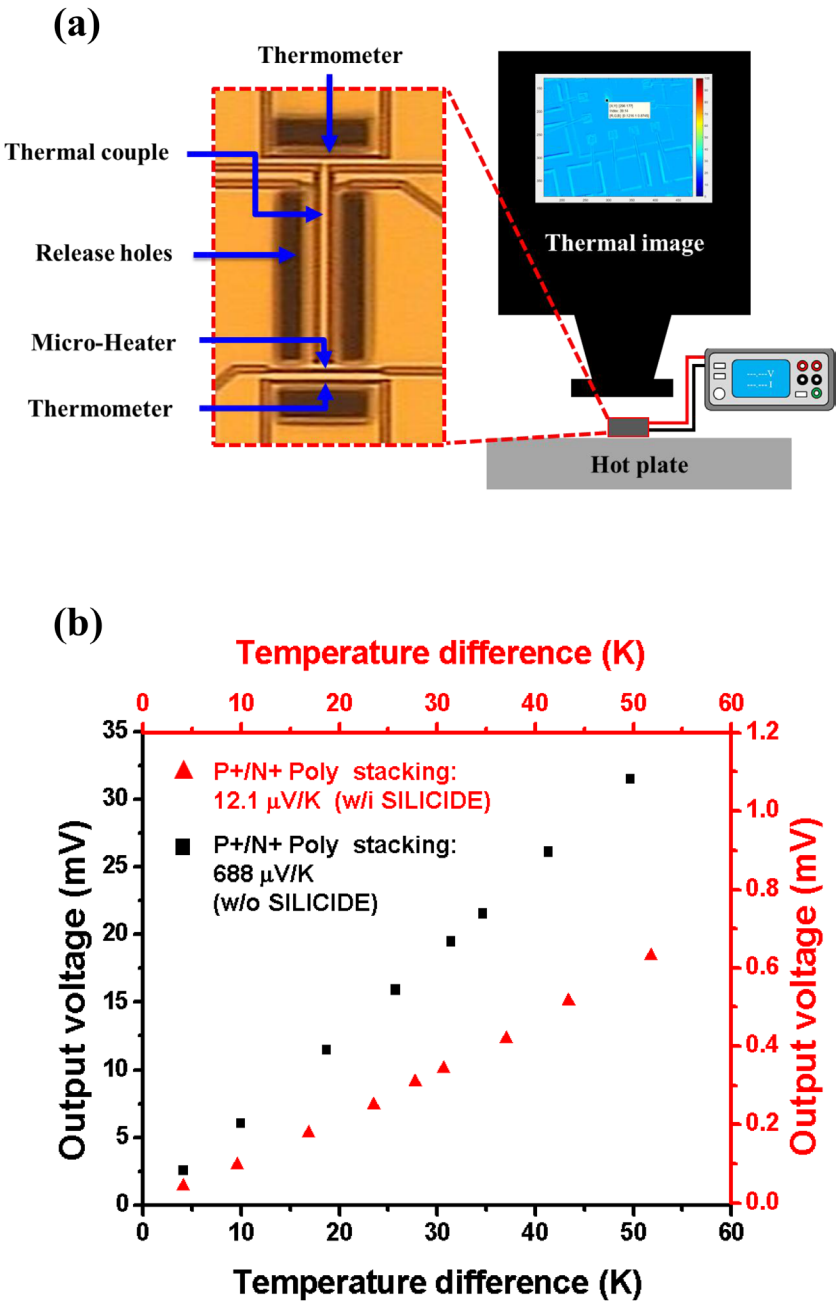

Figure 8. The characterization of Seebeck coefficient: (a) the measurement setup includes the thermal imager, hot plate, and source meter, and the micrograph shows the test-key formed by thermocouple, micro-heater, and thermometers; and (b) the measured output voltages from thermocouples versus temperature variation to determine the Seebeck coefficient.

α of semiconductor can be adjusted by the doping concentration of Si [32]. In addition to the poly-Si layer doped with N^+/P^+, this study also investigated the influence of silicide layer for the presented IR sensor. Note that the silicide layer is used to reduce the electric resistance of poly-Si layer and the contact resistance between poly-Si layer and metal via in CMOS process. The poly-Si films (N^+/P^+) with or without silicide are all available in the standard CMOS process.

The scanning electron microscope (SEM) micrograph in figure 5 shows a typical fabricated chip containing various devices and test structures. As indicated in the micrograph, the proposed and reference IR sensors are implemented on the chip to demonstrate the performance of presented design.

Table 1. The material properties of various poly-Si thin films available in TSMC 0.18 μm 1P6M CMOS process.

Type	α (mV K^{-1})	ρ (mΩm)	κ (W cm^{-1} K^{-1})	Figure of merit
N^+ poly w/i SILICIDE	−5.1	20.6	0.24	5.26
P^+ poly w/i SILICIDE	6.3	20.6	0.24	8.03
N^+ poly w/o SILICIDE	−313	850	0.24	480.24
P^+ poly w/o SILICIDE	286	850	0.24	400.96

Moreover, to evaluate the size effect of presented design, the sensors of two different foot prints (204 × 204 μm^2 and 120 × 120 μm^2) are also fabricated. The test-key is designed

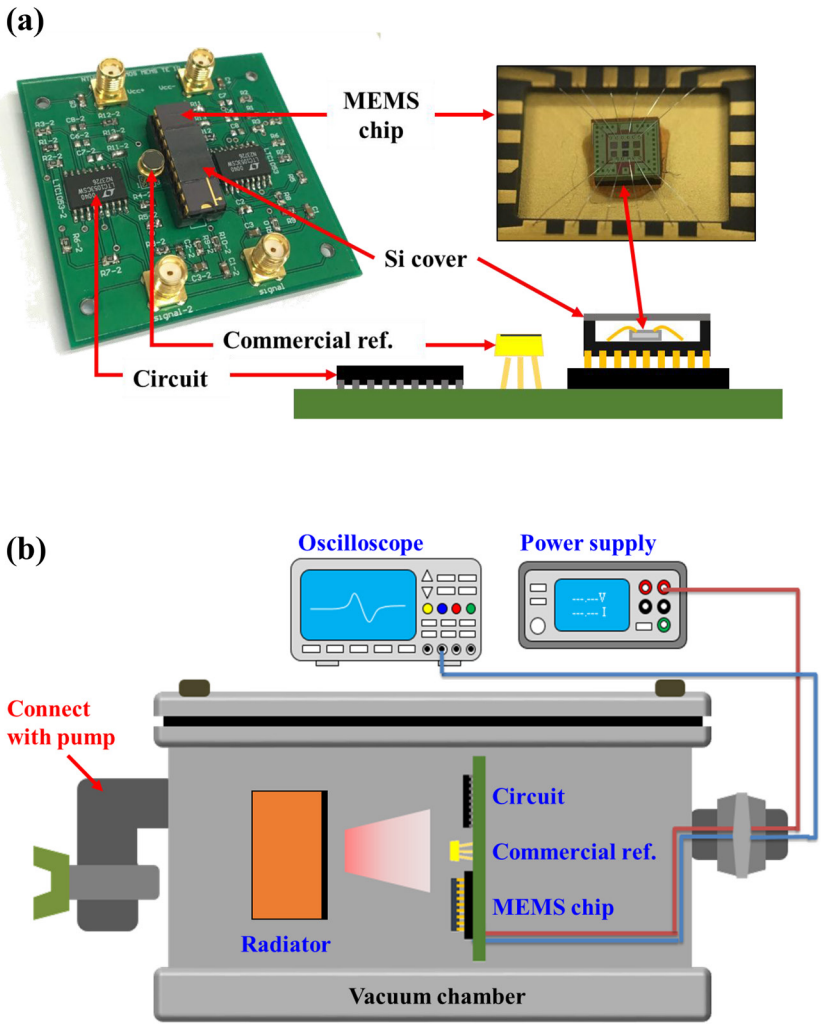

Figure 9. (a) The DUT includes the CMOS-MEMS chip, commercial sensor for calibration, and sensing circuit; and (b) the test setup to measure the responsivity at different ambient pressure.

to characterize the Seebeck coefficient of the sensing film. The zoom-in SEM micrograph in figure 6(a) shows the overview of proposed IR sensor design with umbrella-like absorber structure. After removed the umbrella-like absorber, the serpentine thermopile is observed, as displayed by the zoom-in micrograph in figure 6(b). The cross section micrograph in figure 6(c) depicts the shielding plate anchored at the serpentine structure via the post, and the gap between shielding plate and thermopile can be clearly observed. The zoom-in micrograph in figure 6(d) further displays the stacking of multi-layers and the poly-Si film from standard CMOS process, and the release holes for post-CMOS process. As indicated in figure 7(a), the cross-section prepared by focus-ion-beam (FIB) further displays the shielding plate (~6 μm thick), post, and the thermal isolation air gap (~3.2 μm thick). The surface profiles of shielding plate and thermopile were characterized using the non-contact optical interferometer. The measured profiles (from the 204 $\times$ 204 μm^2 proposed sensor) in figure 7(b) depict that the radius-of-curvature (ROC) of shielding plate is 25.68 mm (black-curve) and the maximum deformation of thermopile profile (red-curve) is 2 μm. The results agree reasonably with the prediction from FEM. Since a near 3.2 μm gap was the design objective in this study, the shielding plate and serpentine thermopile make no contact ensuring thermal isolation by the air gap.

4. Measurements and discussions

Various experiments have been performed in this study to verify the presented design. The Seebeck coefficient of available thin film materials for thermocouple in TSMC 0.18 μm 1P6M CMOS processes have been characterized first for sensor design. In addition, the sensor performances such as the responsivity, response time, and field of view are measured. Finally, according to the measurements, the NEP and detectivity (D^*) can be further determined from equations (5) and (6). The measurement results are summarized in table 2. Note that the experiments were performed under constant temperature and humidity.

4.1. Seebeck coefficient

The test-key and measurement setup to determine the Seebeck coefficient of thermocouple are displayed in figure 8(a). As depicted in figure 5, the test-key structures are monolithically

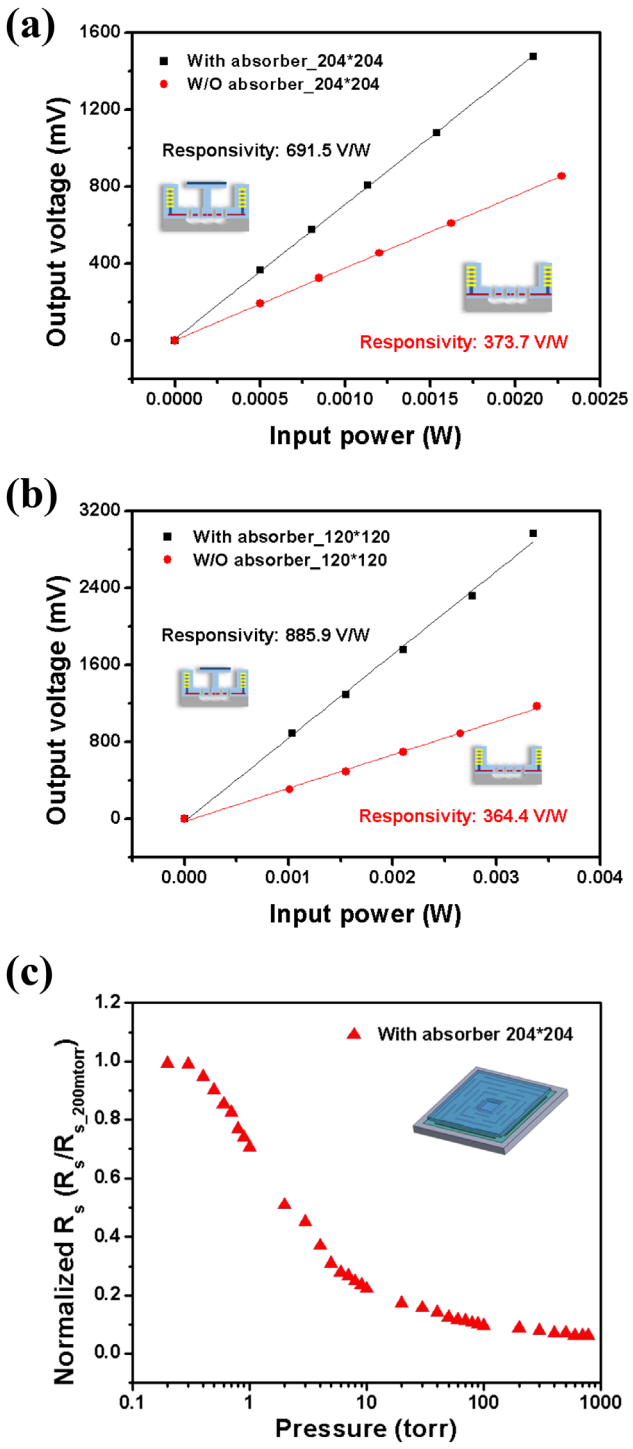

Figure 10. Measurement results of proposed IR sensors, (a) output voltage versus input power for the sensor with 204 × 204 μm^2 footprint at 200 mTorr ambient pressure, and the responsivity is determined from the slope of measurements, (b) output voltage versus input power for the sensor with 120 × 120 μm^2 footprint at 200 mTorr ambient pressure, and (c) variation of responsivity with the ambient pressure for the sensor with 204 × 204 μm^2 footprint.

fabricated with the presented sensors using the CMOS-MEMS processes. Micrograph in figure 8(a) depicts the test-key structure [23, 25] which is formed by a suspended bridge (for thermal isolation) with embedded thermocouple. The thermocouple consists of the poly-Si (N^+/P^+) films to be measured.

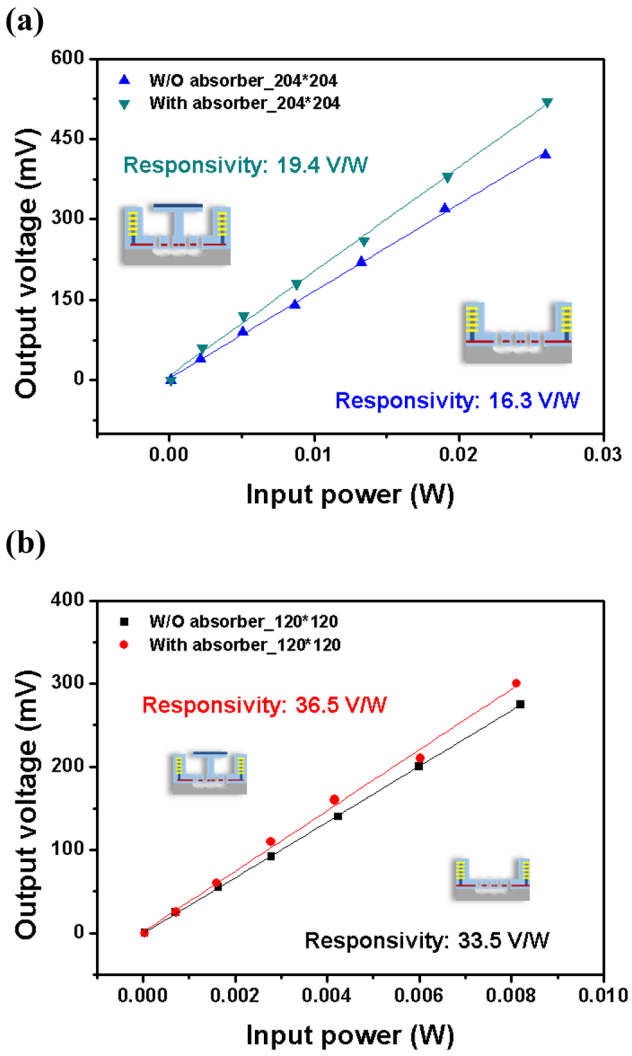

Figure 11. Variation of output voltage with input power for proposed IR sensors at 1 atm, (a) for the sensor with 204 × 204 μm^2 footprint, (b) for the sensor with 120 × 120 μm^2, and the responsivity is determined from the slope of results.

A micro heater is placed at one boundary of the suspended bridge to act as the hot junction, and another boundary of the bridge acts as the cold junction. Moreover, the thermometers are fabricated at both ends of the bridge for temperature monitoring. Thus, the temperature of both hot and cold junctions are measured by thermometers. As the measurement setup shown in figure 8(a), the hot plate under the chip is used to specify a constant ambient temperature for the testing and calibration of thermometers. The thermal IR microscopy is used to confirm the temperature measured from thermometers and also detect the temperature distribution on the test-key. During the measurements, the hot junction is heated up by micro heater, and the Seebeck coefficient is then determined by the output signals from thermometers and thermocouple.

As discussed in section 3, the poly-Si (N^+/P^+) thermocouple with and without silicide are investigated in this study. Measurement results in figure 8(b) indicate that the Seebeck coefficient of thermocouple composed of poly-Si (N^+/P^+) with silicide is 12.1 $\mu V\ K^{-1}$, and the thermocouple composed of poly-Si (N^+/P^+) without silicide becomes 688 $\mu V\ K^{-1}$.

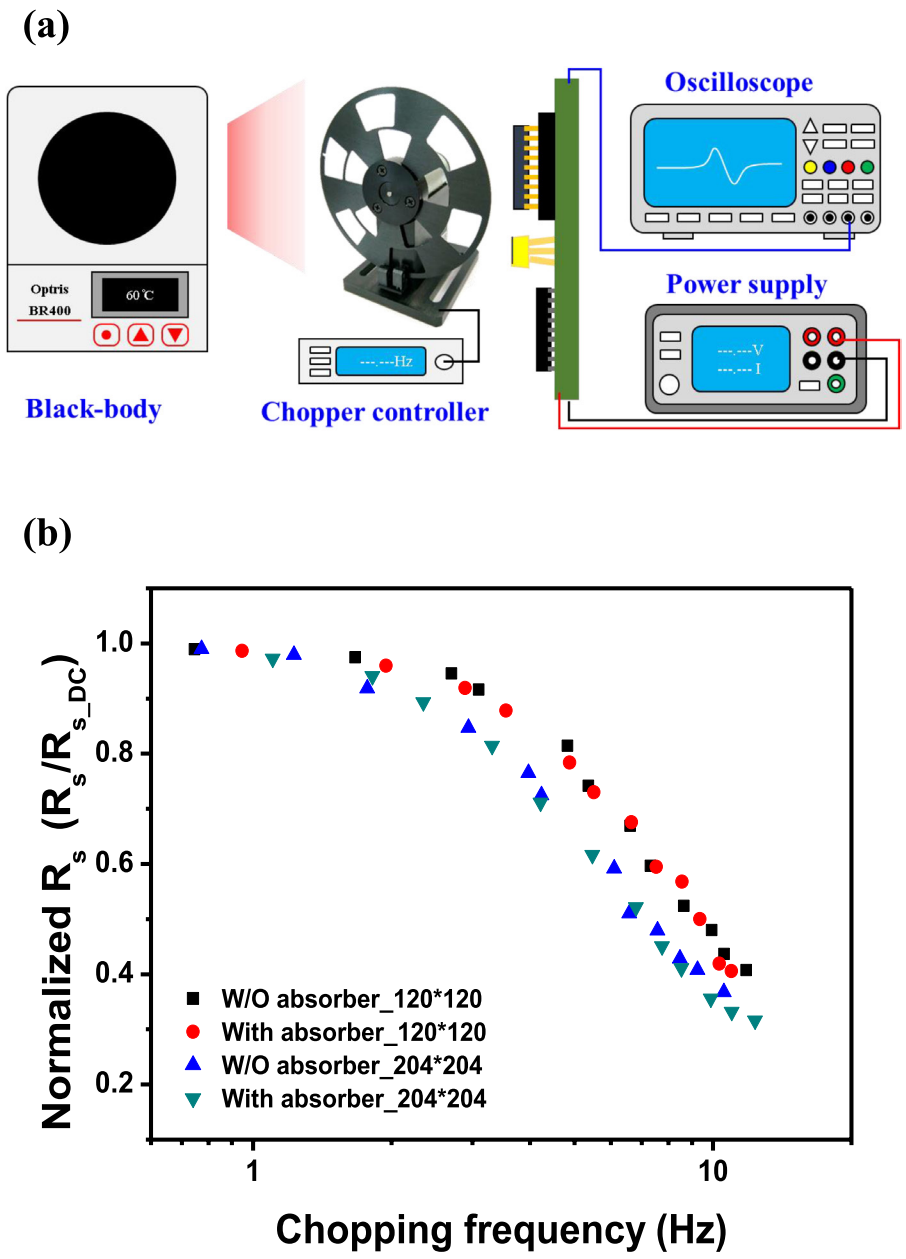

Figure 12. (a) Test setup to measure the thermal time constant of sensors. The optical chopper is employed to adjust the frequency of input IR; and (b) measurement results to depict the variation of responsivity with the chopping frequency, and the thermal time constant of sensors is determined form the cut off frequency.

Thus, for the TSMC 0.18 μm 1P6M CMOS process, the Seebeck coefficient of poly-Si thermocouple is increased for 56-fold by removing the silicide layer. The detailed material properties of poly-Si are summarized in table 1. According to equation (8), the figure of merit of the poly-Si (N^+/P^+) is significantly improved after removing the silicide layer. In summary, this study employed the poly-Si (N^+/P^+) without silicide for the thermocouple.

4.2. Responsivity

Figure 9(a) shows the DUT (device-under-test) including the fabricated chip wire bonded in the ceramic house covered with a Si optical filter, the sensing circuit, and a commercial IR sensor for performance calibration. The test setup in figure 9(b) is established to characterize the performance of IR sensors at different working pressure. The DUT in figure 9(a) is placed inside the vacuum chamber with an IR radiator for testing. The radiator is employed to emit the radiation, and the sensor has an output voltage signal after absorbing the heat radiation. The power of IR is monitored by a commercial IR sensor, and the voltage output from the presented sensor is recorded by the oscilloscope. Measurements in figure 10(a) show the variation of the output voltage and the input power for proposed and reference sensor designs with a foot print of 204 × 204 μm^2. The measurement is performed under an ambient pressure of 200 mTorr. According to equation (3), the responsivity R_s is determined from the slope of the curve in

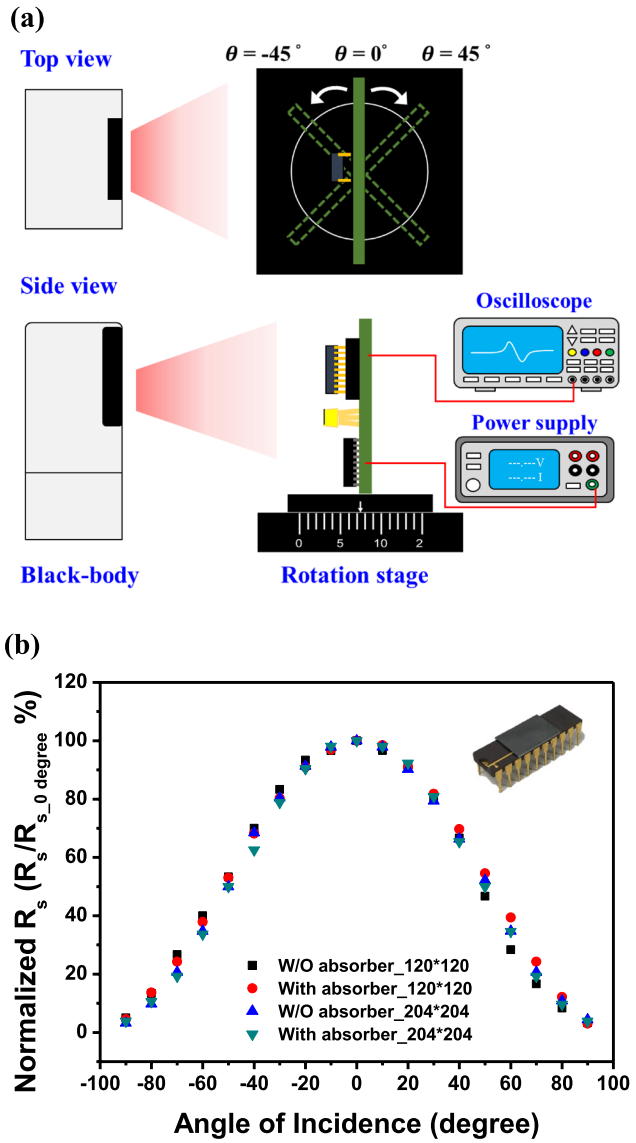

Figure 13. (a) Test setup for the measurement of field of view, the rotation stage is used to control the incident angle of IR; and (b) measurement results to show the normalized responsivity versus the incident angle.

figure 10(a). Thus, the responsivity R_s of proposed and reference designs are respectively 691.5 V W^{-1} and 373.7 V W^{-1} at 200 mTorr. Figure 10(b) further show the measurements for sensors with a foot print of 120 × 120 μm^2. In this case, the responsivity R_s of proposed and reference designs are respectively 885.9 V W^{-1} and 364.4 V W^{-1} at 200 mTorr. The results indicate that the responsivity of proposed design is enhanced to near 1.85-fold for sensor of 204 × 204 μm^2 foot print and near 2.43-fold for sensors of 120 × 120 μm^2 foot print. Measurements in figure 10(c) depict the normalized responsivity ($R_s/R_{s\_200\,\mathrm{mTorr}}$) of proposed design as the ambient pressure varying from 200 mTorr to 1 atm. Due to the heat loss through air conduction, the responsivity of presented sensor is decreased as the ambient pressure is increased.

The results in figure 11 depict the variation of the output voltage and the input power for proposed and reference sensor designs measured at 1 atm. As indicated in figure 11(a), the responsivity of proposed design with a foot-print of 204 × 204 μm^2 is 19.4 V W^{-1}, and the reference design is 16.3 V W^{-1}. Figure 11(b) shows that the responsivity of proposed design with a foot-print of 120 × 120 μm^2 is 36.5 V W^{-1}, and the reference design is 33.5 V W^{-1}. The results can confirm 120 × 120 μm^2 sensors have better heat transduction efficiency than 204 × 204 μm^2 sensors. However, due to the heat loss of shielding plate to the thermocouple through air conduction (as depicted in figure 10(c)), no significant improvement for the present design as it is operated in 1 atm.

4.3. Thermal time constant

The test setup in figure 12(a) is established to measure the responsivity versus the frequency of radiation emitted from radiator (controlled by chopper), so as to determine the thermal time constant of IR sensor. Measurement results in figure 12(b) show the normalized responsivity (R_s/R_{s_DC}) of four different sensor designs varying with the chopping frequency f_{ch}. As defined in [28], the cut off frequency f_{ch_CF} of sensor can be determined from figure 12(b) as the normalized responsivity dropped to the value of 0.707. Thus, the thermal time constant τ can be extracted from the following equation [31],

$$\tau = \frac{1}{2\pi f_{ch\_CF}}. \tag{9}$$

According to the measurements and equation (9), the thermal time constant τ of the proposed design with 204 × 204 μm^2 foot print is 35 ms, and the reference design with the same foot print is 33 ms. Moreover, the thermal time constant τ of the proposed design with 120 × 120 μm^2 foot print is 26 ms, and the reference design with the same foot print is 25 ms. The proposed design has larger thermal resistance and thermal capacitance, hence the thermal time constant is larger than the reference design. Similarly, the sensor with larger foot print (204 × 204 μm^2) has a higher thermal time constant.

4.4. Field of view

Figure 13(a) shows the test setup to determine the field of view of present sensor. As indicated in figure 9(a), the test device is packaged in a ceramic house and then covered with a Si substrate as the optical filter. The rotation stage is used to control the incident angle of IR radiation. The measurements in figure 13(b) present the normalized responsivity ($R_s/R_{s\_0^\circ}$) versus incident angle for four different sensors. The results indicate these four sensors have very similar field of view.

Table 2. Summary and comparison of performances for different types fabricated CMOS MEMS thermoelectric IR sensors.

Type	Reference	Proposed	Reference	Proposed	unit
Element size	204×204		120×120		μm^2
Resistance	1450		733		kΩ
Number of junctions	8		8		
Responsivity @vacuum	373.7	691.5	364.4	885.9	V W^{-1}
NEP	*0.41*	*0.22*	*0.3*	*0.12*	nW $\sqrt{\text{Hz}}^{-1}$
Detectivity @vacuum	0.46	0.9	0.37	0.95	10^8 cm $\sqrt{\text{Hz}}$ W^{-1}
Response time @1 atm	33	35	25	26	ms

5. Conclusions

This study presented thermoelectric IR sensor designs based on the standard CMOS process. The thermoelectric IR sensor has a heat transduction absorber structure, which providing a heat flow path and also enhancing the absorption efficiency of IR to increase the responsivity. Moreover, the material property of poly-Si in TSMC 0.18 μm 1P6M standard CMOS process is analyzed. The Seebeck coefficient of thermocouple can increase 56-fold by removing the silicide process. The proposed sensor design with two different foot prints have been implemented using the standard TSMC CMOS processes and the in-house post-CMOS MEMS processes. Measurements indicate, with a 200 mTorr ambient pressure, the detectivity of proposed design with 204×204 μm^2 foot print can be increased for two fold; and 2.6 fold for the device with 120×120 μm^2 foot print. The specifications of all designs are summarized at table 2. Note that the vacuum ambient is suggested for a better performance of the proposed IR sensor design. As reported in this study, the bending of suspended structure by thin film residual stress can be reduced by shrinking the footprint of the device. Moreover, the post size of absorber can be reduced for a small footprint device, so as to increase the temperature difference ΔT of thermocouple. Thus, the proposed IR sensor design can be further improved by using the small footprint array devices to replace a single large footprint device.

Acknowledgments

This research has been sponsored in part by the Ministry of Science and Technology of Taiwan under grants MOST 107-2218-E-007-022, MOST 104-2221-E-007-016-MY3, MOST 105-2221-E-007-026-MY3, and MOST 106-2622-8-007-006-TE3. The authors want to appreciate the TSMC and the National Chip Implementation Center (CIC), Taiwan, for supporting CMOS chip manufacturing. The authors also would like to appreciate the Center for Nanotechnology, Materials Science and Microsystems (CNMM) of National Tsing Hua University for providing the process tool.

ORCID iDs

Weileun Fang https://orcid.org/0000-0002-6000-026X

References

[1] www.flir.com/discover/rd-science/cooled-or-uncooled/
[2] Rogalski A 2003 Infrared detectors: status and trends *Prog. Quantum Electron.* **27** 59–210
[3] Daniels A 2010 *Field Guide to Infrared Systems, Detectors, and FPAs* 2nd edn (Bellingham, WA: SPIE) pp 44–100
[4] Eminoglu S, Tanrikulu M Y and Akin T 2008 A low-cost 128×128 uncooled infrared detector array in CMOS process *J. Microelectromech. Syst.* **17** 20–30
[5] www.yole.fr/
[6] Xu D, Xiong B and Wang Y 2010 Self-aligned thermoelectric infrared sensors with post-CMOS micromachining *IEEE Electron Device Lett.* **31** 512–4
[7] Xu D, Xiong B and Wang Y 2010 Design, fabrication and characterization of a front-etched micromachined thermopile for IR detection *J. Micromech. Microeng.* **20** 115004
[8] Van Herwaarden A W and Sarro P M 1986 Thermal sensors based on the Seebeck effect *Sensors Actuators* **10** 321–46
[9] Foote M C 1999 Temperature stabilization requirements for unchopped thermal detectors *AeroSense'99. Int. Society for Optics and Photonics*
[10] Masaki H, Ohta Y and Fukuyama Y 2008 Low-cost thermoselectric infrared FPAs and their automotive applications *Proc. SPIE* **6940** 694032
[11] Socher E, Bochobza-Degani O and Nemirovsky Y 2001 A novel spiral CMOS compatible micromachined thermoelectric IR microsensor *J. Micromech. Microeng.* **11** 574–6
[12] Shen T, Lee Y, Chang K and Fang W 2018 Responsivity enhancement of CMOS-MEMS thermoelectric infrared sensor by heat transduction absorber design *2018 IEEE Micro Electro Mechanical Systems (Belfast, 2018)* pp 29–32
[13] Chang K C, Lee Y C, Sun C M and Fang W 2017 Novel absorber membrane and thermocouple designs for CMOS-MEMS thermoelectric infrared sensor *2017 IEEE 30th Int. Conf. on Micro Electro Mechanical Systems (Las Vegas, NV, January 2017)* pp 1228–31
[14] Muller M, Budde W, Gottfried R, Hubel A, Jahne R and Kuck H 1995 A thermoelectric infrared radiation sensor with monolithically integrated amplifier stage and temperature sensor *Proc. 8th Int. Conf. on Solid-State Sensors and Actuators (Stockholm Sweden, June 1995)* pp 640–3
[15] Baltes H, Brand O, Fedder G K, Hierold C, Korvink J and Tabata O 2005 *CMOS MEMS: Advanced Micro and Nanosystems* vol 2 (Weinheim: Wiley)
[16] Smith J H, Montague S, Sniegowski J J, Murray J R and McWhorter P J 1995 Embedded micromechanical devices for the monolithic integration of MEMS with CMOS *Int. Electron Devices Meeting (Washington, DC, December 1995)*

[17] Fedder G K 2005 CMOS-based sensors *IEEE Sensors Conf. (Irvine, CA, October 2005)* pp 125–8
[18] Tsai M, Sun C, Mao W and Fang W 2016 The CMOS-MEMS 3-axis capacitive accelerometer to meet the commercial specifications *2016 IEEE 29th Int. Conf. on Micro Electro Mechanical Systems (Shanghai)* pp 1002–5
[19] Mao W, Cheng C, Lo S, Chen Y and Fang W 2017 Design and implementation of a CMOS-MEMS microphone without the back-plate *TRANSDUCERS (Kaohsiung)* pp 1037–40
[20] Cheng C, Chang H, Chang C and Fang W 2015 Development of a CMOS MEMS pressure sensor with a mechanical force-displacement transduction structure *J. Micromech. Microeng.* **25** 125024
[21] Yeh S, Chang H and Fang W 2018 Development of CMOS MEMS inductive type tactile sensor with the integration of chrome steel ball force interface *J. Micromech. Microeng.* **28** 044005
[22] Zhou H, Kropelnicki P, Tsai J M and Lee C 2013 CMOS-based thermopiles using vertically integrated double polycrystalline silicon layers *IEEE 26th Int. Conf. on Micro Electro Mechanical Systems (Taipei, Taiwan, January 2013)* pp 429–32
[23] Zhou H, Kropelnicki P, Tsai J M and Lee C 2013 Development of a thermopile infrared sensor using stacked double polycrystalline silicon layers based on the CMOS process *J. Micromech. Microeng.* **23** 065026
[24] Tanaka J, Shiozaki M, Aita F, Seki T and Oba M 2014 Thermopile infrared array sensor for human detector application *IEEE 27th Int. Conf. on Micro Electro Mechanical Systems (San Francisco, CA, January 2014)* pp 1213–6
[25] Zhou H, Kropelnicki P and Lee C 2015 CMOS compatible midinfrared wavelength-selective thermopile for high temperature applications *J. Microelectromech. Syst.* **24** 144–54
[26] Chen C N, Huang W C, Chen C C and Shen S H 2009 A novel CMOS-compatible polysilicon/titanium thermopile *IEEE Int. Conf. on Nano/Molecular Medicine and Engineering* pp 158–63
[27] Xu D, Xiong B, Wang Y and Li T 2011 Robust array-composite micromachined thermopile IR detector by CMOS technology *IEEE Electron Device Lett.* **32** 1761–3
[28] Modarres-Zadeh M J and Abdolvand R 2014 High-responsivity thermoelectric infrared detectors with stand-alone sub-micrometer polysilicon wires *J. Micromech. Microeng.* **24** 125013
[29] de Oliveira M J 2017 *Equilibrium Thermodynamics* 2nd edn (Berlin: Springer)
[30] Chen C N 2011 Temperature error analysis and parameter extraction of an 8–14 μm thermopile with a wavelength-independent absorber for tympanic thermometer *IEEE Sens. J.* **11** 2310–7
[31] Cheng C, Tsai M and Fang W 2015 Determining the thermal expansion coefficient of thin films for a CMOS MEMS process using test cantilevers *J. Micromech. Microeng.* **25** 025014
[32] Geballe T and Hull G 1955 Seebeck effect in silicon *Phys. Rev.* **98** 940–7